

# Nanostructured high-strength molybdenum alloys with unprecedented tensile ductility

G. Liu<sup>1</sup>, G. J. Zhang<sup>1,2</sup>, F. Jiang<sup>1</sup>, X. D. Ding<sup>1</sup>, Y. J. Sun<sup>1</sup>, J. Sun<sup>1,3</sup>\* and E. Ma<sup>1,3,4</sup>\*

**The high-temperature stability and mechanical properties of refractory molybdenum alloys are highly desirable for a wide range of critical applications. However, a long-standing problem for these alloys is that they suffer from low ductility and limited formability. Here we report a nanostructuring strategy that achieves Mo alloys with yield strength over 800 MPa and tensile elongation as large as ~40% at room temperature. The processing route involves a molecular-level liquid-liquid mixing/doping technique that leads to an optimal microstructure of submicrometre grains with nanometric oxide particles uniformly distributed in the grain interior. Our approach can be readily adapted to large-scale industrial production of ductile Mo alloys that can be extensively processed and shaped at low temperatures. The architecture engineered into such multicomponent alloys offers a general pathway for manufacturing dispersion-strengthened materials with both high strength and ductility.**

Molybdenum (Mo) is a refractory metal that keeps its body-centred cubic (bcc) crystal structure from room temperature all the way to its high melting temperature of 2,610 °C. Alloys based on Mo offer high stability, high creep resistance and high thermal conductivity, and are thus very attractive for many important high-temperature applications (including as critical components in missiles, turbines and fusion reactors)<sup>1–3</sup>. However, although Mo is inherently strong and hardening to high strength levels is easy in Mo alloys, they do suffer from a major drawback: their limited ductility at temperatures near room temperature (which is also an indicator of inadequate ductility at moderately elevated temperatures). At room temperature, the commercial-purity Mo metal (hereafter abbreviated as CP-Mo, see composition analysis in Table 1) usually offers a uniform tensile elongation of only a few per cent (curve I in Fig. 1a,b; ref. 4). The inadequate ductility is in fact a well-known bottleneck that limits the widespread engineering application of Mo alloys<sup>5–7</sup>. In the nuclear field, for example, the low ductility and radiation-induced embrittlement are the main concerns<sup>3,8,9</sup>.

Improving the ductility at temperatures close to room temperature has been a major goal over recent decades for Mo alloys<sup>3,5</sup>. One approach is to improve the plastic-flow properties of Mo by adding rhenium (Re) as a solute element, which effectively facilitates dislocation motion<sup>10,11</sup>. But this approach causes softening and is costly owing to the expensive Re. A major source of the low ductility of Mo alloys (and some other bcc alloys) is their sensitivity to some solutes unavoidable in commercial products, such as O and N, especially when these impurities segregate at grain boundaries<sup>5,12</sup>. Approaches that modify the grain boundaries and solute distributions<sup>13–15</sup> thus have influences on the strength and ductility. In this regard, second-phase particles (for example, carbide and oxide)<sup>6,14</sup> can play a major role. They can refine the grains by promoting grain nucleation and hindering grain growth. The refined microstructure will result in not only a significant increase in strength, but also abundant grain boundary areas that can drive down the concentration of deleterious solutes in the lattice.

Rare-earth oxide particles are particularly effective<sup>15</sup> because they also gather solutes owing to strong rare-earth–oxygen interactions. The addition of rare-earth oxide has been reported to reduce the grain size from several tens of micrometres in pure Mo to several micrometres in oxide dispersion-strengthened (ODS) Mo alloys<sup>6,15</sup>. We have reproduced the same result, following the conventional processing route of sintering powder blends of solid Mo-based powders mixed with solid oxide powders (that is, a S–S doping route), or mixed with a liquid rare-earth solution (S–L doping, as illustrated for La oxide in Fig. 2a)<sup>15–17</sup>. The resulting Mo alloy with La oxide particles will be referred to as ODS-Mo hereafter. Its microstructure, shown in the transmission electron microscopy (TEM) micrograph in Fig. 3a and in the schematic in Fig. 2a, is similar to what has been reported before for ODS-Mo alloys. The tensile properties of the ODS-Mo are also consistent with those reported in earlier publications (curve II in Fig. 1): the strength elevation is significant (compared with curve I), together with some minor increment in ductility.

The ductility achieved, however, remains inadequate. A major reason for this is that the oxide particles themselves tend to distribute to the grain boundaries. Such a microstructure (again, Figs 3a and 2a) is expected for the S–L mixing processing route, as explained in the Methods. These hard particles introduce stress concentrations at the grain boundaries and tend to localize strains and cracking near them, as demonstrated in Fig. 3b–d, which illustrates crack formation, particle decohesion and particle fracture. This explains the behaviour shown in Fig. 1a (curve II): the ODS-Mo alloy had fine grains and hence a high yield strength, but the elongation was endangered by the initiation of voids/cracks at La<sub>2</sub>O<sub>3</sub> particles located at the grain boundaries<sup>17</sup>.

## Hierarchical microstructure and L–L doping process

The key to prolonged ductility is, therefore, to split these oxide particles into nanosized ones and spread them into the grain interior, rather than having them coarsened and concentrated at the grain boundaries. This strategy not only alleviates the

<sup>1</sup>State Key Laboratory for Mechanical Behavior of Materials, Xi'an Jiaotong University, Xi'an 710049, China, <sup>2</sup>School of Materials Science and Engineering, Xi'an University of Technology, Xi'an 710048, China, <sup>3</sup>Center for Advancing Materials Performance from the Nanoscale (CAMP-Nano), State Key Laboratory for Mechanical Behavior of Materials, Xi'an Jiaotong University, Xi'an 710049, China, <sup>4</sup>Department of Materials Science and Engineering, Johns Hopkins University, Baltimore, Maryland 21218, USA. \*e-mail: junsun@mail.xjtu.edu.cn; ema@jhu.edu.

**Table 1 | Composition of the CP-Mo.**

Composition	Fe	Ni	Al	Si	Ca	Mg	P	C	O	N	Mo
Weight (ppm)	14	0.79	0.69	2.3	4.0	0.82	≤10	9.6	34	2.4	Balance

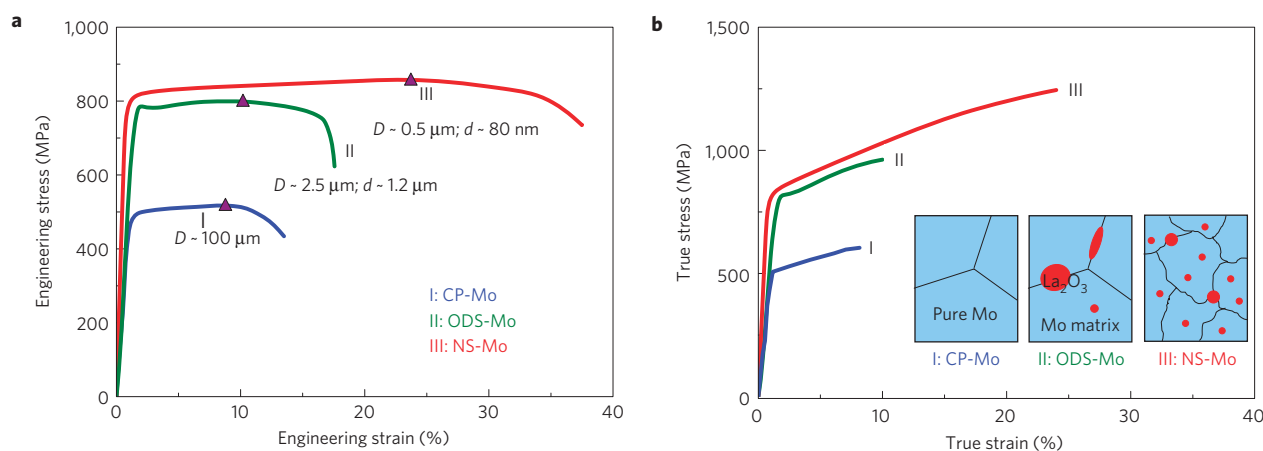


**Figure 1 | Comparison of room-temperature tensile behaviour for three different types of Mo alloys. a, b**, Tensile engineering (a) and true (b) stress–strain curves of CP-Mo with grain size  $D \sim 100 \mu\text{m}$  (ref. 4), ODS-Mo alloy with grain size  $D \sim 2.5 \mu\text{m}$  and oxide particle size  $d \sim 1.2 \mu\text{m}$  (ref. 17), and NS-Mo alloy with grain size  $D \sim 0.5 \mu\text{m}$  and oxide particle size  $d \sim 80 \text{nm}$ . Standard textbook equations are used to convert the engineering stress–strain in a to the true stress–strain in b, up to the point where the sample cross-sectional area becomes non-uniform, that is, for the uniform part of the elongation before necking sets in at the point marked by triangles in a. Plotting true stress versus true strain in b clearly demonstrates the pronounced work hardening at large strains during the tensile deformation of the NS-Mo alloy. Insets in b are sketches illustrating the microstructure in samples corresponding to curves I, II, and III, respectively.

problem discussed in the preceding paragraph, but also encourages dislocation trapping by the particles in the grain interior, which would help sustain work hardening and uniform elongation. In the following, we demonstrate an innovative processing route using liquid–liquid (L–L) blends to achieve this goal. A schematic of the process is shown in Fig. 2b. The processing is readily applicable to mass production and industrial applications, and the details are presented in the Methods section. In essence, the L–L process ensures mixing on the molecular level, and encourages heterogeneous nucleation to form core–shell structures. The outcome is a nanostructured Mo alloy (referred to as NS-Mo hereafter) with nanoscaled  $\text{La}_2\text{O}_3$  particles mostly distributed inside the interior of ultrafine-grained (UFG) Mo crystals; see the TEM image of the microstructure in Fig. 3e. These NS-Mo alloys exhibit an unprecedented combination of strength and ductility: the yield strength is  $\sim 820 \text{MPa}$  and the total tensile elongation to failure is as large as  $\sim 38\%$  (curve III in Fig. 1a). In the meantime, improvements are also obvious in the fracture toughness and ductile-to-brittle transition (Table 2). As such, our strategy offers a nanostructuring design pathway towards ultra-strong and highly ductile materials that occupy an unprecedented regime in the property–performance space.

We will now present details of the microstructure to explain that our processing indeed produced the desired architecture of grains and dispersions, which is different from that of conventional ODS-Mo alloys. This will set the stage for us to explain the properties resulting from the NS-Mo microstructure. Figure 3e shows a representative TEM image of the NS-Mo alloy to compare with the microstructure of ODS-Mo (Fig. 3a). The average grain size is about  $0.5 \mu\text{m}$  for the former, and about  $1.4 \mu\text{m}$  for the latter (the grains in Fig. 3a are smaller than this average, see Fig. 4a). The L–L doping process is apparently more effective in refining the grain structure. The distribution and size of  $\text{La}_2\text{O}_3$  particles are also radically different for the two alloys. In the NS-Mo alloy, most

of the  $\text{La}_2\text{O}_3$  particles are on the nanoscale (average  $\sim 80 \text{nm}$ ) and homogeneously dispersed in the grain interior, as indicated by solid arrows in Fig. 3e (in this area the particle sizes are smaller than the average found, see Fig. 4). Only a small fraction of them are located at grain boundaries (indicated by open arrows, with average sizes around  $140 \text{nm}$ ; more images are shown in Supplementary Fig. S1). A summary of the statistical analysis results on the particle spacing distribution for both the intragranular and intergranular particles is presented in Supplementary Fig. S2. In comparison, for the ODS-Mo alloy the  $\text{La}_2\text{O}_3$  particles are predominantly distributed at grain boundaries (average  $\sim 230 \text{nm}$  in size, indicated by open arrows in Fig. 3a) and very few of them are within grains (see Supplementary Fig. S2). The statistical distribution of the size of the grains, and of the oxide particles, is plotted in Fig. 4; the differences between the two alloys are apparent. More characterization results and statistical information collected from numerous grains and particles regarding the different microstructural features and length scales in the NS-Mo and ODS-Mo alloys are described in the Supplementary Information (see for example Supplementary Table S1).

### Extraordinary tensile ductility

As a result of the different microstructure, compared with the ODS-Mo made of the same starting raw material, our L–L doping method results in significant rises in both strength and ductility: the NS-Mo alloy reaches a strength level in the range of  $800\text{--}900 \text{MPa}$  (Table 2) and a total elongation to failure of  $\sim 40\%$ . The simultaneous high strength and extraordinary ductility set the present alloy apart from all the previously reported submicron-grained or micrometre-grained Mo alloys, which have either low strength or low ductility (or both low), including pure Mo (refs 4,18), Mo–Re (refs 19,20), low carbon arc cast (LCAC) Mo (ref. 17), Mo–Ti–Zr (TZM-Mo; refs 17,20), OSD Mo–Re alloys<sup>15</sup>, and ODS Mo (refs 17,18,21); see the comparisons summarized in Fig. 5, which highlights the unprecedented properties of the NS-Mo alloy that set the latter

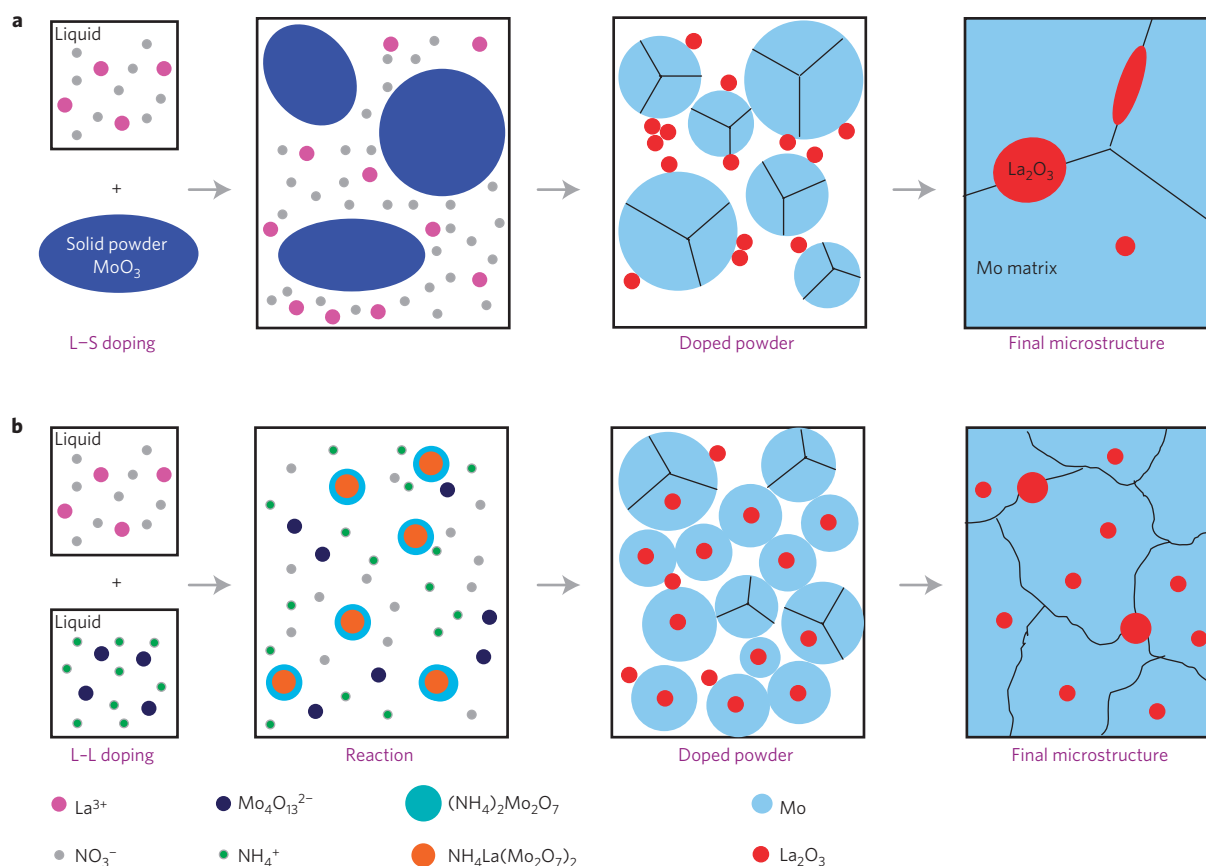


**Figure 2 | Comparison of (L-L) mixing and liquid-solid (L-S) mixing processes and resulting microstructures. a, b,** Schematics showing the microstructural development in the L-S mixing/doping (**a**) and L-L mixing/doping (**b**) processes that produced the ODS-Mo and NS-Mo alloys, respectively. For the L-L process in **b**, note the intimate mixing on molecular level, the heterogeneous nucleation leading to core-shell structures, and the eventual distribution of oxide particles mostly in the grain interior.

apart from all previous Mo alloys. Note that the two TZM-Mo alloys that have yield strength  $\sim 1,000$  MPa were prepared by using spark plasma sintering and hot isostatic pressing, respectively. These two sintering approaches can produce samples with only small sizes and therefore are unsuitable for industrial mass production.

The NS-Mo alloy has a starting recrystallization temperature of  $\sim 1,400$  °C, about 100 °C and 450 °C higher than that of ODS-Mo and CP-Mo, respectively. High-temperature ( $> 1,000$  °C) tensile properties (tensile strength and elongation) of the NS-Mo are also generally better than the best ones published previously for Mo alloys<sup>4,6,17</sup>; see comparisons in Table 3. In particular, the NS-Mo alloys have an elongation of at least 15% at temperatures above 600 °C, which is much higher than the  $< 7\%$  of all previously reported Mo alloys with similar strengths. As such, the present NS-Mo alloy is expected to have deep-drawing capability from room temperature to high temperatures, as well as good stability and service performance at elevated temperatures.

### Mechanisms for high strength and extraordinary ductility

We now analyse the origin of the high strength and extraordinary ductility of the newly developed NS-Mo alloys. Generally speaking, these properties arise from the microstructures we designed and actually produced through the L-L doping process. Specifically, the high strength is expected from the UFG grains and nanoscale particles (see Supplementary Fig. S3), and the excellent ductility is associated with intragranular  $\text{La}_2\text{O}_3$  nanoparticles that help with the generation and storage of dislocations without initiating cracks localized at grain boundaries (see Supplementary Fig. S4).

We first discuss the high strength as a direct consequence of the ultrafine grains derived from the L-L doping technique illustrated in the schematic shown in Fig. 2b. For the conventional L-S mixing case in Fig. 2a, Mo is initially present in the  $\text{MoO}_3$  solid powders and La as ions in a solution. The Mo powders are produced via a solid  $\rightarrow$  solid transformation from the  $\text{MoO}_3$  powders, and the  $\text{La}_2\text{O}_3$  particles are precipitated from the solution. The resulting Mo powders and  $\text{La}_2\text{O}_3$  particles did interact and the two phases were distinctly separated in the as-mixed condition. The small  $\text{La}_2\text{O}_3$  particles may aggregate, while attaching to the Mo powders through physical binding. During sintering, the Mo grains grow through Ostwald ripening. The Zener drag effect imposed by  $\text{La}_2\text{O}_3$  particles hinders the grain-boundary migration to some extent, and the eventual grain size is several micrometres<sup>17</sup>. Furthermore, the  $\text{La}_2\text{O}_3$  particles located between Mo powders coalesce such that they usually have a relatively large size owing to the aggregation and coarsening effects.

In the L-L doping case (Fig. 2b), in contrast, Mo is now present in liquid solution, which promotes the homogeneous mixing of the Mo and La ions. Reactions begin from the precipitation of  $\text{NH}_4\text{La}(\text{Mo}_2\text{O}_7)_2$ . Subsequently,  $(\text{NH}_4)_2\text{Mo}_2\text{O}_7$  is induced to nucleate heterogeneously on  $\text{NH}_4\text{La}(\text{Mo}_2\text{O}_7)_2$ , forming a core-shell structure. This ubiquitous core-shell structure is thermodynamically stable and substantially increases the number of Mo nuclei in the following reactions. Moreover, the core-shell structure keeps the enclosed  $\text{La}_2\text{O}_3$  particles isolated in the Mo grain interior, impeding the  $\text{La}_2\text{O}_3$  particle aggregation and restricting the size of the  $\text{La}_2\text{O}_3$  particles to the nanometre scale. This is the reason that the  $\text{La}_2\text{O}_3$  particles in the NS-Mo alloy have an average size

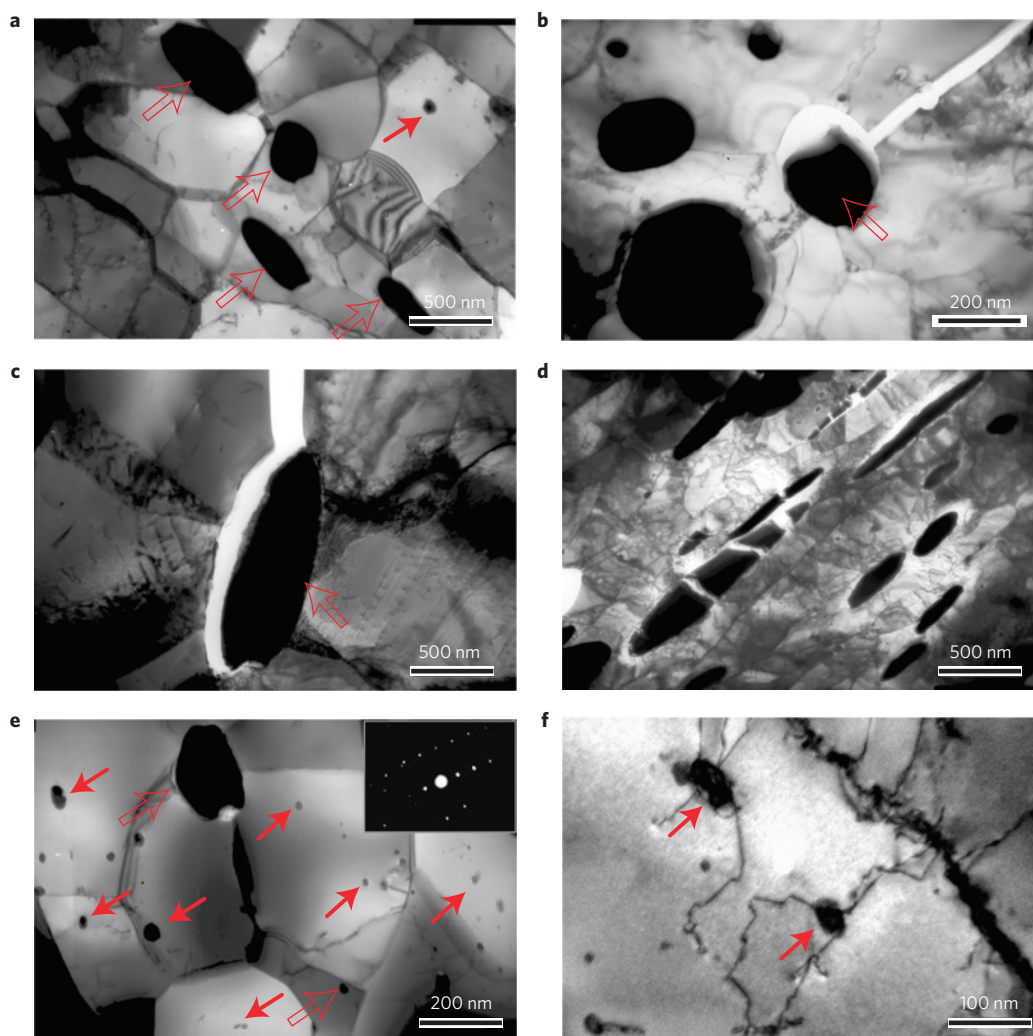


**Figure 3** | TEM images showing the microstructures of ODS-Mo and NS-Mo. **a–f**, Representative TEM images showing the microstructure of ODS-Mo (**a–d**) and NS-Mo (**e,f**). **a**, Mo grains and  $\text{La}_2\text{O}_3$  particles in the ODS-Mo before tensile test. **b**, Cracking at grain boundary caused by intergranular  $\text{La}_2\text{O}_3$  particles. **c**, Particle decohesion. **d** Particle fracture (note the broken particles). **e**, Mo grains and  $\text{La}_2\text{O}_3$  particles in the NS-Mo before the tensile test. The inset shows the selected area diffraction pattern of the  $\text{La}_2\text{O}_3$  particles. **f**, In the deformed sample, dislocations interact with intragranular particles, resulting in pinning and accumulation of dislocations inside the grain. The intergranular  $\text{La}_2\text{O}_3$  particles are indicated by open arrows, and intragranular ones by solid arrows.

**Table 2** | Summary of room-temperature properties of NS-Mo and other Mo alloys.

Alloy	CP-Mo (ref. 4)	ODS-Mo (ref. 17)	NS-Mo
Average grain size ( $\mu\text{m}$ )	$97 \pm 8$	$1.4 \pm 0.7$	$0.5 \pm 0.3$
Yield strength (MPa)	385	$710 \pm 37$	$813 \pm 3$
Ultimate tensile strength (MPa)	534	$746 \pm 49$	$865 \pm 5$
Elongation to failure (%)	13	$14.1 \pm 6.5$	$37.5 \pm 3.0$
Fracture toughness ( $\text{MPa m}^{1/2}$ )	$24.2 \pm 2.3$	52.8	$121.5 \pm 3.5$
DBTT ( $^{\circ}\text{C}$ )	25 (ref. 15)	-60	-100

smaller than those in the ODS-Mo alloy. Because the numerous nanosized particles interact with the migrating grain boundaries, the Mo grains get to stay at small sizes of only  $\sim 0.5 \mu\text{m}$ . Ultrafine Mo grains and optimized  $\text{La}_2\text{O}_3$  particles (reduced in size and predominantly dispersed within grains) are the most important microstructural features of the L–L doping-derived NS-Mo alloy. These refined microstructural scales contribute to the high strength to the alloy, as explained quantitatively using modelling equations and plots in Supplementary Fig. S3.

We next explain in more detail the extraordinary tensile ductility of NS-Mo seen in Fig. 1. We note that both the uniform elongation, that is, the strain achieved before the stress reaches the maximum point where the necking instability begins, and the total elongation to failure have drastically improved over ODS-Mo. UFG and NS structures usually do not bode well for a large uniform elongation<sup>22–24</sup>. One reason is that strain hardening tends to be absent owing to the inability to accumulate dislocations in these tiny crystals<sup>25</sup>. Some strategies have been proposed<sup>24,26</sup> to

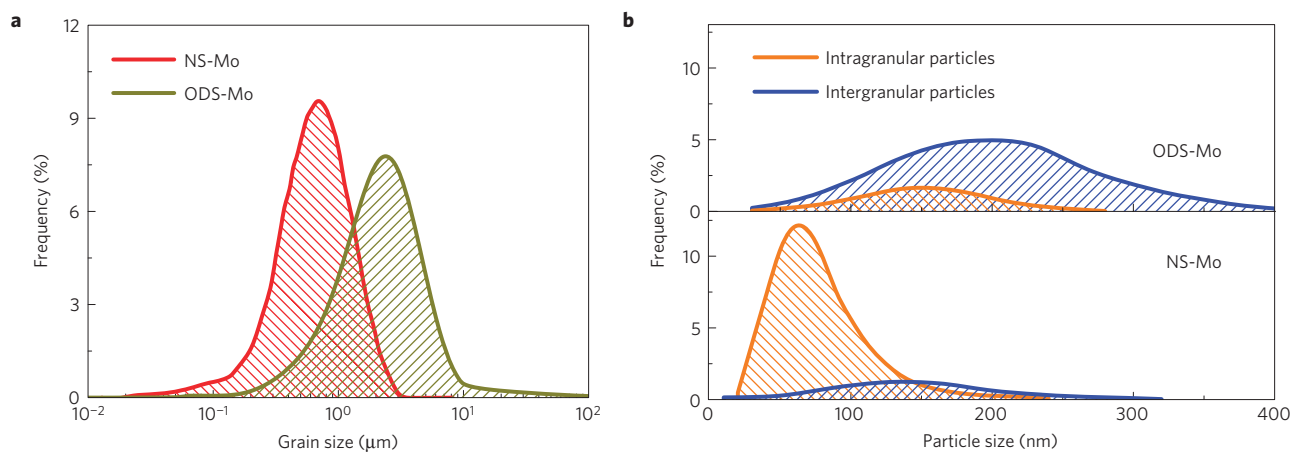


**Figure 4 | Distribution of grain and particle sizes.** **a,b**, Grain size distribution (**a**) and  $\text{La}_2\text{O}_3$  particle size (**b**) distribution in the ODS-Mo and NS-Mo alloys. Note that the particles in the NS-Mo are predominantly in the grain interior rather than at the grain boundaries as in the ODS-Mo.

improve the tensile ductility of bulk NS metals, including bimodal microstructure<sup>24</sup> and grain-boundary design derived from severe plastic deformation<sup>26</sup>. In particular, dispersing nanosized particles in the grain interior is an effective approach to increase the strength and simultaneously improve the ductility of UFG alloys, because the intragranular particles can generate, pin down and thus accumulate dislocations within the grains. This approach was applicable to age-hardenable alloys such as UFG Al alloys<sup>23,27</sup>, in which the nanosized particles precipitate out during the ageing treatment. Here our L–L doping-based preparation method is advantageous in that nanosized  $\text{La}_2\text{O}_3$  particles are borne out of chemical reactions on their own, and predominantly dispersed in the grain interior to serve the dual purposes of blocking dislocations and storing dislocations. The dislocation pinning and accumulation are clearly seen in the TEM image in Fig. 3f: one observes that multiple dislocations interact with intragranular  $\text{La}_2\text{O}_3$  nanoparticles and are either generated around the particles or pinned by the particles (see Supplementary Fig. S1). During tensile deformation the retention of an increasing number of dislocations in the grain interior gives rise to the work hardening observed in the tensile curve in Fig. 1. To clearly observe that work hardening is pronounced over a wide strain range, especially at large strains and high stresses, we have converted the engineering stress–strain curve in Fig. 1a to the true stress versus true strain curve shown in Fig. 1b. The high strain hardening rate accompanying the elevating stresses seen in the tensile curve is essential for achieving large uniform elongation without pronounced strain localization such as necking<sup>22–24</sup>. In comparison, the dislocation accumulation inside the grains is appreciably lower in the deformed ODS-Mo (see Supplementary Fig. S5), as there the vast majority of the particles reside at the grain boundaries.

Moreover, as discussed earlier, our microstructure also delays failure by reducing the grain-boundary  $\text{La}_2\text{O}_3$  particles both in their sizes and population. The  $\text{La}_2\text{O}_3$  particles at grain boundaries as observed in the ODS-Mo alloy are preferential sites for crack initiation during loading<sup>6,28</sup>. This is because, owing to deformation incompatibility, large stress concentrations will be induced at the particles, inducing interfacial decohesion at the weaker grain boundaries or particle cracking that eventually lead to microcracks along the grain boundaries. As shown earlier, in the L–S doping and sintering process (Fig. 2a) the precipitated  $\text{La}_2\text{O}_3$  particles tend to aggregate to form coarser particles, and most of them reside at grain boundaries. Coarser particles tend to induce a greater severe stress/strain concentration and they are also more likely to break because of lower fracture strength (the fracture strength of particles scales inversely with particle size<sup>29</sup>). Figure 3b–d are TEM images captured in the deformed ODS-Mo, clearly revealing that grain-

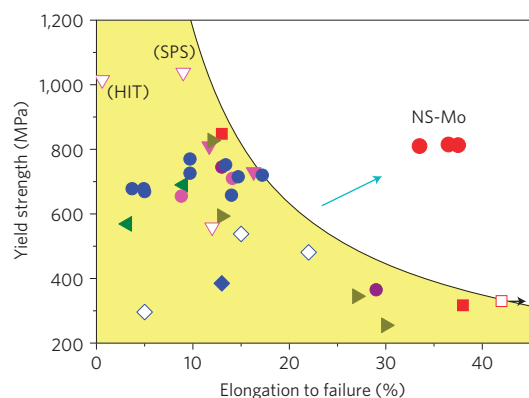


**Figure 5 | Yield strength versus total tensile elongation of NS-Mo in comparison with available literature data.** The present NS-Mo data are shown as red filled circles. The literature data are for all types of representative Mo alloys, including CP-Mo (filled diamond<sup>4</sup> and open diamonds<sup>18</sup>), Mo-Re (filled squares<sup>19</sup> and open squares<sup>20</sup>), LCAC-Mo (filled left triangles<sup>17</sup>), TZM-Mo (filled down triangle<sup>17</sup> and open down triangle<sup>20</sup>), ODS-Mo-Re (filled right triangles<sup>15</sup>), and ODS-Mo (filled pink circles<sup>17</sup>, filled purple circles<sup>18</sup> and filled blue circles<sup>21</sup>). Our NS-Mo alloys with simultaneous high strength and ductility clearly stand out, above and beyond the known trend (the shaded yellow region) for the normal trade-off between strength and ductility. Solid circles are for La oxide strengthened Mo alloys. SPS: spark plasma sintering; HIT: hot isostatic pressing.

boundary  $\text{La}_2\text{O}_3$  particles cause intergranular fracture. The particles are prone to decohesion and fracture during processing or loading (Fig. 3c,d), degrading the ductility. For the L–L doping process, in contrast, the  $\text{La}_2\text{O}_3$  particles are isolated within core–shell structures (Fig. 2b). This ensures that the  $\text{La}_2\text{O}_3$  particles are mainly retained within grains after sintering. As a result, in the NS-Mo alloy  $\text{La}_2\text{O}_3$  particles are smaller in size, and few and far between at grain boundaries (see Fig. 3e). This alleviates the propensity for intergranular fracture and thus increases the total elongation before failure. These results emphasize again that in Mo alloys grain boundaries should be carefully tailored to reach high ductility.

The fracture toughness of the NS-Mo is also considerable higher than the CP-Mo or ODS-Mo, as measured at room temperature using the three-point bending technique and fatigue pre-cracked specimens. A quantitative comparison is presented in Table 2. The ductile-to-brittle transition temperatures (DBTT) are also compared. The NS-Mo exhibits a much lower DBTT of  $\sim 100^\circ\text{C}$  (in

**Table 3 | High-temperature tensile properties of Mo alloys.**

Alloys	Properties			
	Tensile strength (MPa)/elongation (%)			
	1,000 °C	1,200 °C	1,300 °C	1,400 °C
CP-Mo	120/8.6*	102/6.4	88/7.2	72/5.8
ODS-Mo	382/10.7*	205/8.7	184/11.4	167/9.6
NS-Mo	368/23.7*	224/28.8	211/25.4	185/22.7
TZM-Mo (ref. 17)	520/3.6	414/5.6	-	172/26
LCAC-Mo (ref. 17)	260/2.7	-	-	-
ODS-Mo (ref. 17)	313/4.9	-	-	-

\*Measured at 1,050 °C.

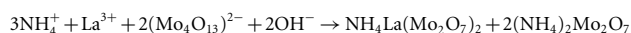
accord with an extrapolation, from a known correlation of DBTT with grain size<sup>15,30</sup>, to a refined grain size of ~500 nm).

### Concluding remarks

In this work we have designed, and successfully manufactured, a hierarchical microstructure in ODS Mo alloys, via the development of a L–L mixing process that enables the control of grains and dispersions in a nanostructured regime. An unprecedented tensile ductility, in terms of both the total elongation to failure and the uniform elongation (both almost tripling that of CP-Mo; see Fig. 1 and Table 2), has been derived from the resulting NS-Mo alloy, together with a real advance in formability revealed by actual trials (a wire drawing case demonstrating the advantage of the NS-Mo alloy is shown in Supplementary Fig. S6 as an example). The lack of ductility and toughness is no longer a bottleneck problem for these Mo alloys. Our findings will also help guide endeavours to architecture other dispersion-strengthened alloys to simultaneously elevate strength and ductility. For example, a similar nanostructuring strategy is expected to be equally effective for other refractory materials, such as tungsten alloys.

### Methods

Our NS-Mo alloys were prepared using a molecular-level liquid–liquid (L–L) mixing/doping process<sup>31</sup>, as illustrated in Fig. 2b in comparison with the conventional route of L–S mixing/doping in Fig. 2a. In this L–L doping, lanthanum oxide (La<sub>2</sub>O<sub>3</sub>) was firstly dissolved into an aqueous solutions of nitrate (La(NO<sub>3</sub>)<sub>3</sub>). This solution is then mixed with another liquid solution, one that contains ammonium molybdate. In the resulting L–L mixture (pH = 8–9) the overall chemical reaction is



The reaction starts from the precipitation of NH<sub>4</sub>La(Mo<sub>2</sub>O<sub>7</sub>)<sub>2</sub> solid powders, uniformly distributed in the solution. Subsequently, (NH<sub>4</sub>)<sub>2</sub>Mo<sub>2</sub>O<sub>7</sub> is induced to nucleate heterogeneously on top of NH<sub>4</sub>La(Mo<sub>2</sub>O<sub>7</sub>)<sub>2</sub>, forming a core–shell structure. Heating at 450 °C for 1 h decomposes these powders into molybdenum oxide enclosing the La oxide. These powders were immediately reduced into molybdenum powder in dry hydrogen, with La oxide embedded inside, see Fig. 2b. The powders were subsequently squeezed into a cylindrical compact (17 mm in diameter) via cold isostatic pressing, and then sintered at 1,850 °C for 6 h in flowing dry hydrogen. Subsequently, the cylindrical compact was thermomechanically processed into a rod with a diameter of 7.8 mm, starting from rolling at 1,500 °C, followed by five steps of warm rolling at successively decreasing temperatures from 1,400 to 300 °C with an average cross-sectional reduction of about 10% per step<sup>31</sup>. Finally, the rod was annealed at 1,250 °C in a dry hydrogen atmosphere for 1 h to relieve residual stress and stabilize the microstructure.

In comparison, conventional ODS-Mo alloys were prepared via the liquid–solid (L–S) doping process, shown in Fig. 2a. Solid molybdenum oxide powder (mostly MoO<sub>3</sub>) is wet doped with a lanthanum nitrate solution. The slurry is dried in air and given a heat treatment in hydrogen at 1,050–1,100 °C for 4.5 h to reduce the molybdenum oxide and pyrolyze the lanthanum nitrate. This process results in a nominal 0.6 wt% content of La<sub>2</sub>O<sub>3</sub> in the powder. Other procedures are the same as in preparing the NS-Mo rods.

The mass fraction of La<sub>2</sub>O<sub>3</sub> is ~0.6 wt% in both NS- and ODS-Mo alloys. Several batches of samples were prepared to ensure repeatability. CP-Mo was also

prepared using the molybdenum oxide powder, following similar sintering and rolling procedures. The chemical composition of CP-Mo is listed in Table 1.

Microstructure of the alloys was characterized by means of TEM, before and after tensile tests. The foils for TEM observations were produced by electropolishing in a twin-jet apparatus with a solution of 12.5 vol.% H<sub>2</sub>SO<sub>4</sub> in ethanol at –15 °C. A voltage of 10 V produced a current density of 3 mA mm<sup>–2</sup>. The grain sizes in both the cross-sectional and longitudinal direction have been determined and the average grain size was obtained from measurements on about 500 grains. The particle size, spacing, and volume fraction of both intergranular and intragranular particles have been statistically analysed using quantitative metallography<sup>32–34</sup> based on ~4,000 intragranular and ~200 intergranular particles in the NS-Mo alloy, and ~300 intergranular and ~700 intergranular particles in the ODS-Mo alloy.

By heating the specimens at progressively elevated temperatures from 800 to 1,500 °C in a vacuum of about 1.4 × 10<sup>–4</sup> Pa, the recrystallization temperature was determined to be the critical temperature at which the grains show significant growth after holding for 1 h.

Room-temperature tensile tests were performed using a servohydraulic Instron-1195 testing machine at a constant strain rate of 1.3 × 10<sup>–4</sup> s<sup>–1</sup>. The dog-bone shaped tensile specimens had a gauge size of 5 mm in diameter and 25 mm in length. The ductile-to-brittle transition temperature (DBTT) of the alloys was measured by uniaxially loading the tensile specimen to failure at temperatures ranging from 200 to 196 °C at a strain rate of 0.05 min<sup>–1</sup>, to compare with the DBTT of previous alloys tested in the same way. The DBTT was identified as the lowest test temperature at which no evidence of brittle cleavage fracture was observed on the fracture surface.

The fracture toughness was measured by means of three-point bending tests, using fatigue pre-cracked samples with *a/W* value of 0.55–0.65 (*a* is the crack length and *W* the sample width) and specimen dimensions of 20 mm in length and 5 mm in width/thickness. The room-temperature properties of the present NS-Mo alloys are summarized in Table 2, in comparison with other previously reported Mo alloys.

High-temperature tensile tests were conducted on a Gleebe 1500D at a strain rate of 10<sup>–1</sup> s<sup>–1</sup> at temperatures between 1,050 and 1,400 °C. The high-temperature tensile properties are compared with previous Mo alloys in Table 3.

Received 3 September 2012; accepted 5 December 2012;  
published online 27 January 2013

### References

- Perepezko, J. H. The hotter the engine, the better. *Science* **326**, 1068–1069 (2009).
- Dimiduk, D. M. & Perepezko, J. H. Mo-Si-B alloys: Developing a revolutionary turbine-engine material. *Mater. Res. Soc. Bull.* **9**, 639–645 (2003).
- El-Genk, M. S. & Tournier, J. M. A review of refractory metal alloys and mechanically alloyed-oxide dispersion strengthened steels for space nuclear power systems. *J. Nucl. Mater.* **340**, 93–112 (2005).
- Sturm, D. *et al.* The influence of silicon on the strength and fracture toughness of molybdenum. *Mater. Sci. Eng.* **463**, 107–114 (2007).
- Wadsworth, J., Nieh, T. G. & Stephens, J. J. Recent advances in aerospace refractory-metal alloys. *Int. Mater. Rev.* **33**, 131–150 (1988).
- Cockeram, B. V. The fracture toughness and toughening mechanism of commercially available unalloyed molybdenum and oxide dispersion strengthened molybdenum with an equiaxed, large grain structure. *Metall. Mater. Trans.* **40A**, 2843–2860 (2009).
- Schneibel, J. H., Brady, M. P., Krucic, J. J. & Ritchie, R. O. On the improvement of the ductility of molybdenum by spinel (MgAl<sub>2</sub>O<sub>4</sub>) particles. *Z. für Metall.* **96**, 632–637 (2005).

8. Cockeram, B. V., Smith, R. W., Hashimoto, N. & Snead, L. L. The swelling, microstructure, and hardening of wrought LCAC, TZM, and ODS molybdenum following neutron irradiation. *J. Nucl. Mater.* **418**, 121–136 (2011).
9. Byun, T. S., Li, M., Cockeram, B. V. & Snead, L. L. Deformation and fracture properties in neutron irradiated pure Mo and Mo alloys. *J. Nucl. Mater.* **376**, 240–246 (2008).
10. Trinkle, D. R. & Woodward, C. The chemistry of deformation: How solutes soften pure metals. *Science* **310**, 1665–1667 (2005).
11. Medvedeva, N. I., Gornostyrev, Y. N. & Freeman, A. J. Solid solution softening and hardening in the group-V and group-VI bcc transition metals alloys: First principles calculations and atomistic modelling. *Phys. Rev. B* **76**, 212104 (2007).
12. Brosse, J. B., Fillet, R. & Biscondi, M. Intrinsic intergranular brittleness of molybdenum. *Scr. Metall.* **15**, 619–623 (1981).
13. Miller, M. K., Kenik, E. A., Mousa, M. S., Russell, K. F. & Bryhan, A. J. Improvement in the ductility of molybdenum alloys due to grain boundary segregation. *Scr. Metall.* **46**, 299–303 (2002).
14. Majumdar, S., Raveendra, S., Samajdar, I., Bhargava, P. & Sharma, I. G. Densification and grain growth during isothermal sintering of Mo and mechanically alloyed Mo-TZM. *Acta Mater.* **57**, 4158–4168 (2009).
15. Mueller, A. J., Bianco, R. & Buckman, R. W. Evaluation of oxide dispersion strengthened (ODS) molybdenum and molybdenum-rhenium alloys. *Inter. J. Ref. Met. Hard Mater.* **18**, 205–211 (2000).
16. Zhang, G. J. *et al.* Microstructure and strengthening mechanism of oxide lanthanum dispersion strengthened molybdenum alloy. *Adv. Eng. Mater.* **6**, 943–948 (2004).
17. Cockeram, B. V. The mechanical properties and fracture mechanisms of wrought low carbon arc cast (LCAC), molybdenum-0.5pct titanium-0.1pct zirconium (TZM), and oxide dispersion strengthened (ODS) molybdenum flat products. *Mater. Sci. Eng. A* **418**, 120–136 (2006).
18. Bianco, R. & Buckman, R. W. Jr *et al.* in *Molybdenum and Molybdenum Alloys* (ed. Crowson, A.) 125–44 (TMS, 1998).
19. Klopp, W. D. & Witzke, W. R. Mechanical properties of electron-beam-melted molybdenum and dilute Mo–Re alloys. *Metall. Trans.* **4**, 2006–2008 (1973).
20. Takida, T. *et al.* Mechanical properties of fine-grained, sintered molybdenum alloys with dispersed particles developed by mechanical alloying. *Mater. Trans. JIM* **45**, 143–148 (2004).
21. Cockeram, B. V. Measuring the fracture toughness of molybdenum-0.5 pct titanium-0.1 pct zirconium and oxide dispersion-strengthened molybdenum alloys using standard and subsized bend specimens. *Metall. Mater. Trans. A* **33A**, 3685–3707 (2002).
22. Wang, Y. M., Chen, M. W., Zhou, F. H. & Ma, E. High tensile ductility in a nanostructured metal. *Nature* **419**, 912–915 (2002).
23. Zhao, Y. H., Liao, X. Z., Cheng, S., Ma, E. & Zhu, Y. T. Simultaneously increasing the ductility and strength of nanostructured alloys. *Adv. Mater.* **18**, 2280–2283 (2006).
24. Ma, E. Eight routes to improve the tensile ductility of bulk nanostructured metals and alloys. *JOM* **58**, 49–53 (2006).
25. Kumar, K. S., Van Swygenhoven, H. & Suresh, S. Mechanical behaviour of nanocrystalline metals and alloys. *Acta Mater.* **51**, 5743–5774 (2003).
26. Sabirov, I., Murashkin, M. Yu. & Valiev, R. Z. Nanostructured aluminium alloys produced by severe plastic deformation: New horizons in development. *Mater. Sci. Eng. A* **560**, 1–24 (2013).
27. Sha, G., Wang, Y. B., Liao, X. Z., Duan, Z. C., Ringer, S. P. & Langdon, T. G. Influence of equal-channel angular pressing on precipitation in an Al–Zn–Mg–Cu alloy. *Acta Mater.* **57**, 3123–3132 (2009).
28. Wadsworth, J., Packer, C. M., Chewey, P. M. & Coons, W. C. A microstructural investigation of the origin of brittle behaviour in the transverse direction in Mo-based alloy bars. *Metall. Trans.* **15A**, 1741–1752 (1984).
29. Gurland, J. & Plateau, J. The mechanism of ductile rupture of metals containing inclusions. *Trans. Am. Soc. Metals* **56**, 442–454 (1963).
30. Cockeram, B. V. The role of stress state on the fracture toughness and toughening mechanisms of wrought molybdenum and molybdenum alloys. *Mater. Sci. Eng. A* **528**, 288–308 (2010).
31. Sun, J., Zhang, G. J., Sun, Y. J., Liu, G., Jiang, F. & Ding, X. D. *A Preparing Method of Mo Alloys Doped with Nanosized Rare-earth Oxides Particles*, Chinese Patent ZL 200810150463.0 (2010).
32. Liu, G., Sun, J., Nan, C. W. & Chen, K. H. Experimental and multiscale modelling of the coupled influence of constituents and precipitates on the ductile fracture of heat-treatable aluminium alloys. *Acta Mater.* **53**, 3453–3468 (2005).
33. Liu, G., Zhang, G. J., Wang, R. H., Hu, W., Sun, J. & Chen, K. H. Heat treatment-modulated coupling effect of multi-scale second-phase particles on the ductile fracture of aged aluminium alloys. *Acta Mater.* **55**, 273–284 (2007).
34. Pauly, S., Liu, G., Gorantla, S., Wang, G., Kuhn, U., Kim, D. H. & Eckert, J. Criteria for tensile plasticity in Cu–Zr–Al bulk metallic glasses. *Acta Mater.* **58**, 4883–4890 (2010).

### Acknowledgements

This work was supported by the National Natural Science Foundation of China (51171149, 51171142, 50831004), the 973 Program of China (No. 2010CB631003), the 863 Key Project of China (No. 2008AA031000), the National Science Technology Supporting Program of China (No. 2012BAE06B02), and the 111 Project of China (B06025). We thank L. Wang and J. H. Luo, from JinDuiCheng Molybdenum, China, for their assistance in the production and application of the NS-Mo alloys. E.M. was supported in part by an adjunct professorship at XJTU.

### Author contributions

J.S. designed and supervised the project, G.J.Z., G.L., F.J. and Y.J.S. carried out the experiments, G.L., X.D.D. and J.S. performed the calculations, E.M., G.L. and J.S. wrote the paper. All the co-authors contributed to discussions.

### Additional information

Supplementary information is available in the [online version of the paper](#). Reprints and permissions information is available online at [www.nature.com/reprints](http://www.nature.com/reprints). Correspondence and requests for materials should be addressed to J.S. or E.M.

### Competing financial interests

The authors declare no competing financial interests.